SANS coupled with fluid invasion approaches for characterization of overall nanopore structure and mesopore connectivity of organic-rich marine shales in China

Yang Wang[1,2], Yanming Zhu[1,2,*], Rui Zhang[3,**], Lawrence M. Anovitz[4], Markus Bleuel[5,6], Shimin Liu[3], and Shangbin Chen[1,2]

[1]Key Laboratory of Coalbed Methane Resources and Reservoir Formation Process, Ministry of Education, China University of Mining and Technology, Xuzhou, Jiangsu 221008, China
[2]School of Resources and Earth Science, China University of Mining and Technology, Xuzhou, Jiangsu 221116, China
[3]Department of Energy and Mineral Engineering, G[3] Center and Energy Institute, Pennsylvania State University, University Park, Pennsylvania 16802, United States
[4]Chemical Sciences Division, Oak Ridge National Laboratory, Oak Ridge, Tennessee 37831, United States
[5]NIST Center for Neutron Research, National Institute of Standards and Technology, Gaithersburg, Maryland 20899, United States
[6]Department of Materials Science and Engineering, A. James Clark School of Engineering, University of Maryland, College Park, Maryland 20742, United States

Corresponding authors:
[*]Email: ymzhucumt@126.com; [**]Email: zhangrui117@gmail.com

Abstract

The pore structure of shales, including pore morphology, connectivity, pore volume, specific surface area (SSA), and pore size distribution (PSD), is a significant factor in controlling gas storage and transport and the migration mechanisms of hydrocarbons. However, the lack of comprehensive characterization for both accessible and inaccessible pore structure increases the difficulty of gas-in-place estimation and gas exploration. In order to investigate the nanoscale pore system, integration of high-pressure mercury intrusion porosimetry (MIP), low-pressure N_2/CO_2 adsorption (LNA/LCA), and small-angle neutron scattering (SANS) were employed to obtain a multi-scale quantitative characterization of the nanopore structure of organic-rich marine shale samples from the Longmaxi and Niutitang Formations in China. PSDs obtained from the combined techniques appropriately cover an overall nanopore size range of shale (0.35-15,000 nm) and overcome the limits of the individual method. Uni-, bi, and multi-modal PSDs were observed, but the sizes of a significant portion of the nanopores observed in these shales

range from 0.35 to 100 nm. Pore volumes and surface areas of micropores (< 2 nm), mesopores (2–50 nm), and macropores (> 50 nm) were characterized based on the best performance window of each technique: LCA for micropores; LNA and SANS for mesopores; and MIP for macropores. It was found that micropores are the major contributor to the total SSA for both Longmaxi and Niutitang shales. With respect to pore volume, however, the contribution to the total pore volume has a trend of micropore < mesopore < macropore for Longmaxi shale samples, but Micro-/mesopore volumes are greater than macropore volumes for samples of the Niutitang shale. Strong correlations were also observed between total organic carbon (TOC) content and micropore volume and surface area, which implies that organic matter is a controlling factor in the micropore system of organic-rich shales. In addition, strong correlations between methane adsorption capacity and both micro-/mesopore volumes and SSAs indicate that micro-/mesopores are governing factors for methane storage. Furthermore, the fractions of accessible mesopore volume and surface area were quantitatively estimated by SANS and LNA. Correlation analyses suggest that the accessibility of the mesopore surface area could be an indicator for gas transport and storage in mesopores in organic matter. Thus, a shale with higher connectivity could have higher gas diffusion capability but lower gas adsorption capacity, and vice versa.

Keywords

Organic-rich marine shale; nanopore structure; mesopore connectivity; small-angle neutron scattering; low-pressure N_2 and CO_2 adsorption

1. Introduction

Shale gas, an important unconventional gas resource, has attracted significant attention in recent years in many parts of the world (Curtis, 2002; Hazra et al., 2018; Jarvie et al., 2007;

Merkel et al., 2016; Ross and Bustin, 2009; Zhao et al., 2016; Zou et al., 2015). The investigation and exploration of shale gas will help meet the rapidly increasing demand for energy consumption worldwide. Environmental pollution from the combustion of natural gas produced in shale gas reservoirs will be less than that caused by burning coal and crude oil. Available data, however, shows that shale gas reservoir rocks are characterized by more complex and more heterogeneous nanoscale pore systems than sandstones and carbonates (Anovitz and Cole, 2015; Chen et al., 2017a; Loucks et al., 2012), making modeling of gas recovery from shale reservoirs more complex. The characterization of these nanoscale pore systems can, therefore, provide insights into hydrocarbon storage capacity and flow mechanisms in shale gas reservoirs (Pearce et al., 2018a; Ross and Bustin, 2009; Wang et al., 2014), as well as improve reservoir modeling (Carlson and Mercer, 1991; Mohaghegh, 2013; Wu et al., 2016) and recovery (Cipolla, 2009; Lee et al., 2011; Wu et al., 2014).

According to the pore classification system of the International Union of Pure and Applied Chemistry (IUPAC) pores in shale can be classified into three groups: macropores (> 50 nm), mesopores (2–50 nm) and micropores (< 2 nm) (Sing, 1985). Multiple qualitative and quantitative techniques have been employed to characterize pore structures in terms of their pore morphology, pore volume, specific surface area (SSA), pore size distribution (PSD), and pore connectivity (Anovitz and Cole, 2015; Li et al., 2016; Liu et al., 2018; Mastalerz et al., 2018; Naveen et al., 2018). Direct imaging, fluid injection, and scattering techniques, including transmission electron microscopy (TEM) (Morga and Pawlyta, 2018; Romero-Sarmiento et al., 2014), field emission scanning electron microscopy (FE-SEM) (Pashin et al., 2012; Topór et al., 2017), low-pressure N_2/CO_2 adsorption (LNA/LCA) (Clarkson et al., 2013; Hazra et al., 2018), mercury intrusion porosimetry (MIP) (Zhang et al., 2017), nuclear magnetic resonance (NMR)

(Webber et al., 2013; Zhou et al., 2016), small-angle X-ray scattering (SAXS) and ultra-/small-angle neutron scattering (USANS/SANS) (Bahadur et al., 2018; Clarkson et al., 2013; Distefano et al., 2019; Gu et al., 2015; Pan et al., 2016; Pearce et al., 2018b; Ruppert et al., 2013; Sun et al., 2018) have been widely used in recent studies. Each of these techniques, however, has its strengths and limitations. LNA/LCA and MIP provide good measurements of pore distributions over a relatively wide size range, but cannot provide information about the percentage of inaccessible or closed pores. TEM and FE-SEM can directly observe pore morphology and identify the pore type, but because of the high magnifications involved can not provide representative and statistically quantitative information. Scattering techniques, including SAXS and SANS, allow for the characterization of both accessible and inaccessible pores but provide limited information on pore morphology and, like diffraction, yield data in inverse space. Therefore, there is an urgent need to thoroughly investigate the nanopore structures using a combination of these techniques (Anovitz and Cole, 2015).

In China, shale gas exploration has been developing for more than a decade and significant progress has been made in shale gas extraction from the Upper Yangtze Platform (UYP) (Chen et al., 2017b; Wang et al., 2018; Yang et al., 2017; Zhao et al., 2016). The Lower Cambrian Niutitang and Lower Silurian Longmaxi shale Formations in the UYP are considered the most promising strata for shale gas exploration in China because of their widespread occurrence, thickness, organic richness, and favorable mineral composition with high quartz content (Chen et al., 2017b; Xiao et al., 2015). In recent years, successful commercialized shale gas production has been achieved from Lower Silurian Longmaxi shales in the Jiaoshiba area of the Fuling Block (Guo, 2016; Zhao et al., 2016). Compared to the Lower Silurian shales, however, exploitation of the Lower Cambrian shales in China has been less successful, though they exhibit

similar geochemical parameters and mineral compositions. While this is likely due to complex shale geology and various reservoir conditions, the exact causes of this failure are unknown.

To date, the lack of an accurate characterization of the nanopore structures of these two shales has been a significant impediment to evaluation of shale gas production and, unfortunately, few studies have been devoted to fully characterizing the differences of nanopore structures between the Longmaxi and Niutitang shales (Sun et al., 2017; Wang et al., 2018; Yang et al., 2017). In this study, therefore, we have integrated SANS with fluid invasion methods including LNA, LCA, and MIP to gain a more comprehensive understanding of the nanoscale pore networks of these two shale Formations. This work will, therefore, have a broad application for improving prediction of gas production potential in Chinese marine shales and bridge the gap between nanopore structure and gas adsorption behavior.

2. Geological Setting

Yangtze platform is a craton basin. Tectonically, the UYP comprises the western part of the Yangtze platform in south China and is enveloped by the Qinling fault belt in the north and the Longmenshan fault belt in the west (Jia et al., 2006; Meng et al., 2005).The UYP is a vast area of approximately $3.5\times10^5 km^2$, including Northern Yunnan Province, Sichuan Province, Guizhou Province, Chongqing City, Western of Hunan and Hubei Province (Fig. 1). The UYP went through multiple periods of tectonic events, such as the late Caledonian - Hercynian movement, Indosinian movement, and Yanshan-Himalayan movement (Liu et al., 2016; Ma et al., 2008). Today, the tectonic characteristics in the study area are mainly showing NE-SW oriented tight anticlines and broad synclines, associated with faults of similar orientation (Tang et al., 2019).

The marine organic-rich shales are widely developed in the UYP, particularly in the Lower Cambrian Niutitang and Lower Silurian Longmaxi Formations. These organic-rich shales were

deposited in a low-energy, quiet, and anoxic marine environment that underwent early burial and later uplifting stages of evolution (Guo and Zhang, 2014). With the increased exploration of shale gas, four Longmaxi Formation gas shale fields have been discovered in the Jiaoshiba, Fushun-Yongchuan, Zhaotong, and Changning-Weiyuan areas in the UYP (Dai et al., 2016). Therefore, the UYP has recently been regarded as the main target for shale gas exploration and development in China.

3. Experimental methods

3.1 Sample collection

A total of six marine shale samples were analyzed in this study, which are the same as those in our previous study (Wang et al., 2018). Four fresh Longmaxi Formation shale core samples were collected from the WX_2 well, located in northeast Chongqing near the edge of the Sichuan Basin. Two fresh Niutitang Formation shale core samples were collected from the QD_1 well, located in northeast Yunnan near the southwestern edge of the UYP (Fig. 1). In order to avoid contamination and keep samples fresh, shale samples were collected from 1538-1625 m for WX_2 well and 1125-1183 m for QD_1 well, respectively. Meanwhile, all samples were carefully and rapidly covered using cling wrap and then brought to the laboratory in opaque bags.

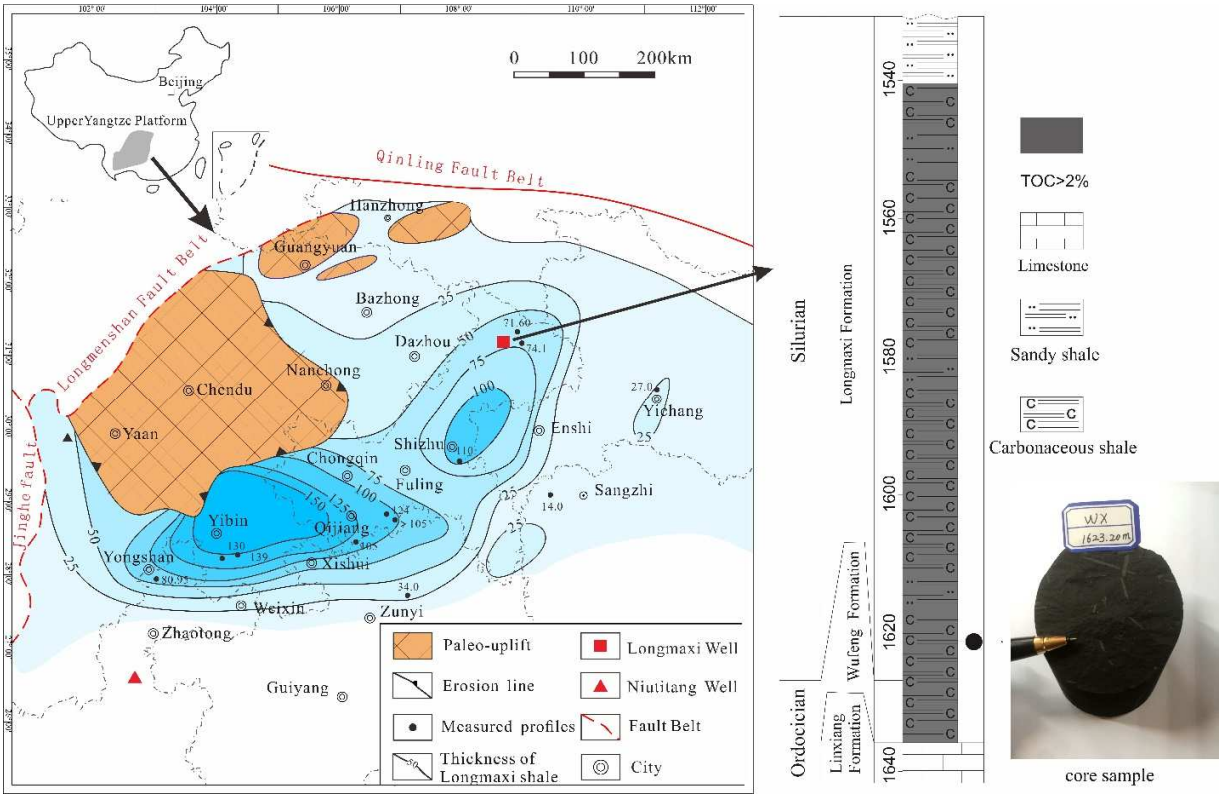

Figure 1. Map of UYP and sampling location (modified after Wang et al., 2018). Note that Contour colors from shallow to deep represent the increase of the thickness of Longmaxi shale. The bottom of the Longmaxi Formation consists of carbonaceous shale. The core sample was collected from a depth of 1623.2 m

3.2 Mercury intrusion porosimetry

MIP analyses were carried out on a Micrometrics AutoPore IV 9510 porosimeter at pressures from 0.14 to 413 MPa. This instrument is located at the China University of Mining and Technology, Xuzhou, Jiangsu, China. Shale samples were cores with diameters of 1 cm and lengths of 1 cm. Before the MIP test, each shale sample was dried at 60 ℃ for more than 48 h and then cooled to room temperature at a relative humidity of less than 10 %. The PSD was calculated from the MIP curve using the Washburn equation (Washburn, 1921).

3.3 FE-SEM observation

FE-SEM was performed with a Quanta 200F equipped with an energy-dispersive spectrometer (EDS) at the State Key Laboratory of Petroleum Resource and Prospecting, China University of Petroleum (Beijing). Prior to the experiment, the surfaces of the measured samples were prepared by Ar-ion milling. The experiment was conducted at a temperature of 24 °C and a humidity level of 35%. SEM images were obtained under high vacuum at 1-20 kV acceleration voltages using the back-scattering electron detector.

3.4 Low-pressure N_2 and CO_2 adsorption

LNA and LCA were measured using a Quantachrome Autosorb-1 apparatus at the China University of Mining and Technology. Powder samples had a particle size of 60-80 mesh. Before adsorption, the powders were degassed at ~110 °C for approximately 24 hours. LNA and LCA isotherms were measured at 77 and 273 K, respectively. The LNA data were interpreted using the multi-point Brunauer–Emmett–Teller (BET) model for estimation of SSA, and the Barrett-Joyner-Halenda (BJH) model for estimations of pore volume and PSD. The LCA data were interpreted using the Dubinin-Astakhov (D-A) model for estimations of micropore volume and surface area, and Density Functional Theory (DFT) for estimation of PSD (Dubinin, 1989; Ross and Bustin, 2009; Chalmers et al., 2012). A detailed description of these theories can be found in Gregg and Sing (1982).

3.5 Small-angle neutron scattering

Six shale samples were analyzed using SANS in this study. Two powder samples denoted WX_2-8 and WX_2-33 were analyzed using the general-purpose SANS (GP-SANS) at the High Flux Isotope Reactor (HFIR) at the Oak Ridge National Laboratory (ORNL). These samples, with a non-uniform particle size of <0.5 mm, were placed in aluminum holders inside stainless-

steel high-pressure cells. Four thin disk samples, approximately 150 μm thick and mounted on quartz glass slides (Anovitz et al., 2009), denoted QD_1-L3, QD_1-L4, WX_2-49, and WX_2-54 were analyzed using the NG7 30m SANS at the NIST Center for Neutron Research (NCNR) at the National Institute of Standards and Technology (NIST). The detailed experimental configurations can be found in our previous study (Wang et al., 2018).

4. Results

4.1 Basic characterization

The geochemical parameters and mineral compositions of the samples are listed in Table 1. The detailed experimental methods of those analyses are shown in our previous study (Wang et al., 2018). The TOC contents of the shale samples range between 1.52 and 6.33 wt.%. The values of the equivalent vitrinite reflectance ($EqVR_r$) range from 2.06 to 3.03 %, indicating that shales in the study area have experienced strong thermal maturation and reached the post-mature stage (Wang et al., 2018). The mineral compositions are dominated by quartz and clay with average contents of 49.3 and 28.9 wt.%, respectively (Wang et al., 2018). Moreover, shale samples also contain several other minerals, including pyrite, calcite, dolomite, K-feldspar, and plagioclase.

Table 1. Basic properties of the tested six shale samples[a]

Formation	Sample ID	Quartz (wt.%)	K-feldspar (wt.%)	Plagioclase (wt.%)	Dolomite (wt.%)	Calcite (wt.%)	Pyrite (wt.%)	Clay (wt.%)	Illite (wt.%)	Smectite (wt.%)	Chlorite (wt.%)	Illite/Smectite mixed layer (wt.%)	TOC (wt. %)	EqVRr (%)
Niutitang ($Є_1$)	QD_1-L3	46.61	4.64	7.25	1.35	5.61	1.64	29.59	15.09	5.03	1.55	7.93	3.29	2.85
	QD_1-L4	54.15	1.44	3.64	nd	6.98	2.39	27.08	19.61	1.15	0.77	5.55	4.32	3.03
Longmaxi (S_1)	WX_2-8	37.42	1.48	14.28	nd	2.17	2.76	40.38	25.90	nd	5.12	9.36	1.52	2.06
	WX_2-33	46.33	nd	9.60	2.94	13.71	3.82	21.54	10.38	nd	2.55	8.62	2.05	2.12
	WX_2-49	49.41	1.15	5.27	nd	3.26	9.10	27.58	16.09	1.53	3.35	6.61	4.25	2.26
	WX_2-54	50.77	3.09	8.43	1.12	3.28	5.99	20.98	13.58	1.12	2.15	4.12	6.33	2.32

[a]Data from Wang et al. (2018); nd is no data.

4.2 Accessible nanopore characterization from invasive methods

4.2.1 Mercury intrusion

The cumulative mercury intrusion and extrusion volumes as a function of pressure for the six shale samples are shown in Fig. 2a. The mercury intrusion volume gradually increases with increasing pressure at relatively low pressure, then rapidly increases with increasing pressure above some relatively high pressure, indicating the presence of macropores and mesopores, respectively. The highest cumulative intrusion volume among the tested samples was that for sample WX_2-54 (yellow cycles in Fig. 2a). Hysteresis was observed between mercury intrusion and extrusion cycles for all the tested samples indicating that approximate 40–90 % of mercury was trapped in the macro-/mesopores.

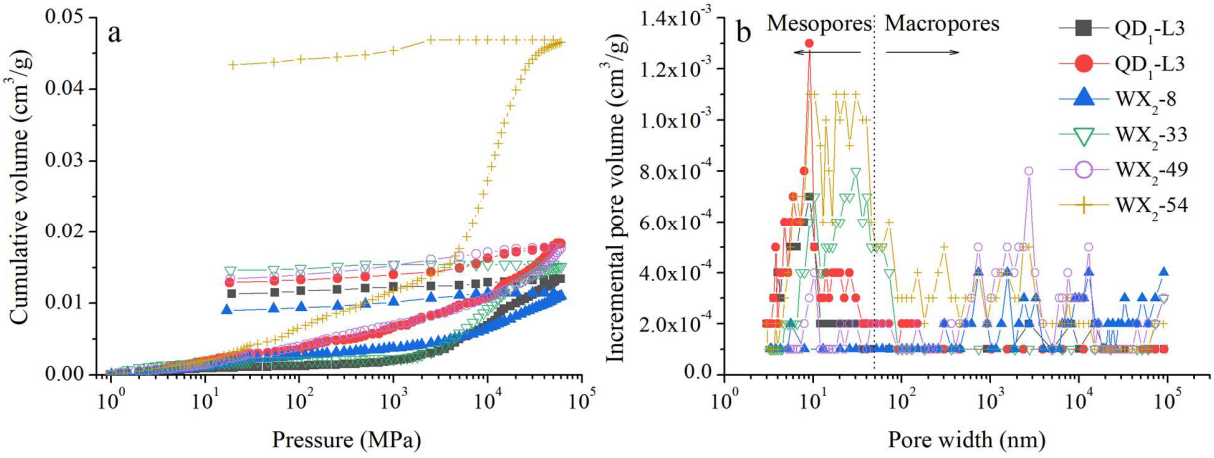

Figure 2. (a) Mercury intrusion/extrusion curves and **(b)** incremental pore volumes.

Table 2 exhibits the results of the pore structure parameters derived from MIP. The MIP results indicate the presence of both uni- and multi-modal PSDs as shown in Fig. 2b. The results suggest that most pores for both the Niutitang and Longmaxi shales have sizes between 5 and 100 nm and are, therefore, classified as macro-/mesopores. The observed PSD variability indicates that there is substantial heterogeneity in pore properties among the tested shale samples. Based on the MIP data, the macropore volume varies from 0.18 to 1.44 cm^3/100g, and the

macropore surface area ranges from 0.006 to 0.199 m^2/g. However, published results suggest that significant populations of the micropores and narrow mesopores in shales are sealed or inaccessible (closed), and thus are not accessible to MIP analysis (Anovitz and Cole, 2015; Kuila and Prasad, 2013).

Table 2. Pore volume and SSA of each method and the overall nanopores

Sample ID	MIP-macropore		LNA-mesopore		LCA-micropore		SANS-mesopore		Overall micro-/meso-/macropores[a]	
	Volume ($cm^3/100g$)	SSA (m^2/g)	Volume ($cm^3/100g$)	SSA (m^2/g)	Volume ($cm^3/100g$)	SSA (m^2/g)	Volume ($cm^3/100g$)	SSA (m^2/g)	Volume ($cm^3/100g$)	SSA (m^2/g)
QD_1-L3	0.18	0.006	0.51	8.32	0.571	16.07	1.33	17.69	1.261	24.396
QD_1-L4	0.31	0.077	0.71	4.53	0.486	14.57	1.20	16.07	1.506	19.177
WX_2-8	1.03	0.044	0.18	1.89	0.086	2.57	0.26	2.39	1.296	4.504
WX_2-33	0.33	0.100	0.21	3.13	0.222	6.25	0.46	4.79	0.762	9.480
WX_2-49	1.31	0.083	1.21	8.52	0.556	15.91	1.49	19.86	3.076	24.513
WX_2-54	1.44	0.199	0.80	10.51	0.931	28.30	3.42	43.62	3.171	39.009

[a]The overall pore properties are from three invasive methods.

4.2.2 Low-pressure N_2 adsorption

The LNA isotherms for shale samples are shown in Fig. 3a. At low relative pressures ($P/P_0 < 0.05$), adsorption capacity increases significantly with increasing P/P_0, suggesting filling of liquid N_2 inside micropores. For P/P_0 values between 0.05 and 0.95, adsorbed volume increases gradually with increasing P/P_0, a behavior associated with mesopore filling of liquid N_2 and capillary condensation. When P/P_0 is greater than 0.95, the adsorption capacity increases rapidly with increasing P/P_0 and does not exhibit any plateau, indicating that both the Niutitang and Longmaxi shales contain macropores and micro-fractures.

Hysteresis loops were observed in all of the adsorption-desorption isotherms as shown in Fig. 3a. The shape of the hysteresis loops may be classified as type H3 according to the IUPAC classification (Sing, 1985), which indicates the presence of abundant slit-shaped pores. This was

supported by SEM imaging (Fig. 3c, 3d). However, pore-shape analysis based on solely adsorption-desorption isotherm shape is clearly idealized, and the actual pore system is likely to be composed of a mixture of different pore shapes, perhaps similar to the irregularly-shaped pores observed in our previous study (Wang et al., 2018).

Over a wide range of P/P_0, LNA analysis can provide information on mesopore structure including mesopore SSA and pore volume (Thommes et al., 2015). As shown in Table 2, the mesopore SSA of the shale samples ranges from 1.89 to 10.51 m^2/g. Sample WX_2-54 contains the highest mesopore SSA, while sample WX_2-8 has the lowest. The mesopore volume varies from 0.51 to 1.21 $cm^3/100g$, and LNA analysis suggested that sample WX_2-49 contains the highest mesopore volume, while sample WX_2-8 again has the lowest.

Fig. 3b shows PSDs (dV/dW versus W, where V is adsorption volume and W is pore width) for the six shale samples obtained from the adsorption branches of the LNA isotherms using the BJH model. The PSD shows a broad range of pore sizes between 1.8 and 100 nm. The PSD displays a decreasing trend in differential pore volume dV/dW with increasing pore size for all tested samples, indicating that the pore concentration decreases with increasing pore size over the measured pore size range. These results are consistent with the mesopore SSA and volume results (Table 2). The mesopore SSA and volume of samples WX_2-49 and WX_2-54 are higher than those of other samples and sample WX_2-8 has the smallest pore volume in the pore diameter range between 2 and 50 nm (Fig. 3b).

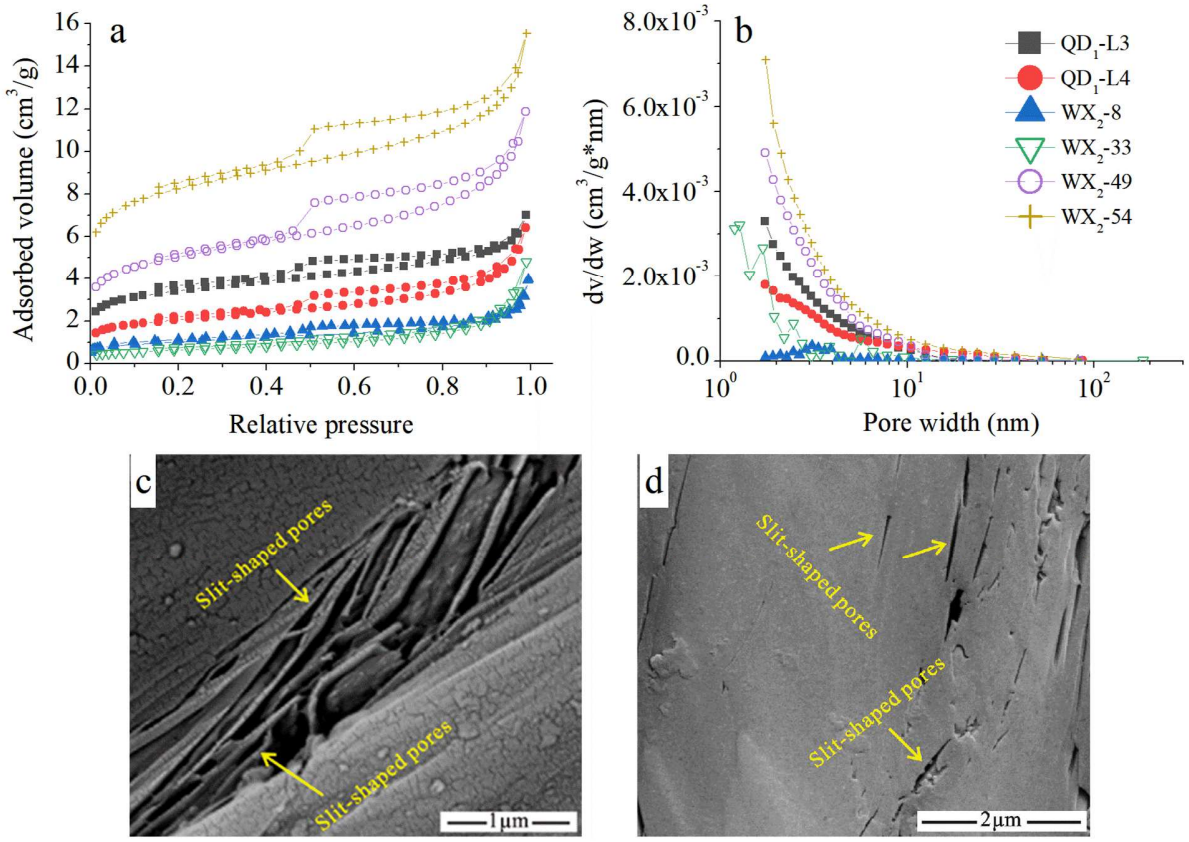

Figure 3. **(a)** Low-pressure N_2 adsorption isotherms, **(b)** differential pore volume distributions, **(c)** sample WX_2-33, and **(d)** sample QD_1-L3 SEM images of slit-shaped pores.

4.2.3 Low-pressure CO_2 adsorption

LCA has been widely used to characterize micropore structure because the accessibility of CO_2 in small pores is better than that of N_2 (Chalmers et al., 2012; Mastalerz et al., 2013; Sun et al., 2016). Fig. 4a shows the CO_2 adsorption isotherms for the six shale samples. These can be classified as Type I (Sing, 1985), indicating that the shales are microporous solids. To obtain information on micropore volume and surface area from the LCA data we used the D-A model (Chalmers et al., 2012; Dubinin, 1989). The results are shown in Table 2. The micropore volume ranged from 0.086 to 0.931 $cm^3/100g$. The micropore surface area ranged from 2.57 to 28.30 m^2/g. Sample WX_2-54 showed the highest micropore volume and surface area, while sample WX_2-8 has the smallest. Micropore PSDs were estimated from LCA using a DFT model (Gregg

and Sing, 1982). The results are shown in Fig. 4b. These show multimodal PSDs in the pore diameter range between 0.35 and 1 nm. A peak occurs between 0.45 and 0.65 nm, and two minor peaks occur around 0.32-0.38 nm and 0.72-0.85 nm, respectively. For pore sizes greater than 1 nm the pore concentration is approximately constant within the micropore size range for each shale. Again, sample WX_2-54 shows the highest dV/dW value, which is consistent with the micropore volume and surface area calculations (Table 2). MIP, N_2, and CO_2 adsorption thus all suggest that this sample has a higher pore volume and surface area than the other five samples at nearly all pore sizes. It also has the highest helium porosity (Wang et al., 2018). Also, for all samples, the pore volume in the micropore range detected by CO_2 adsorption is higher than that detected by N_2 adsorption.

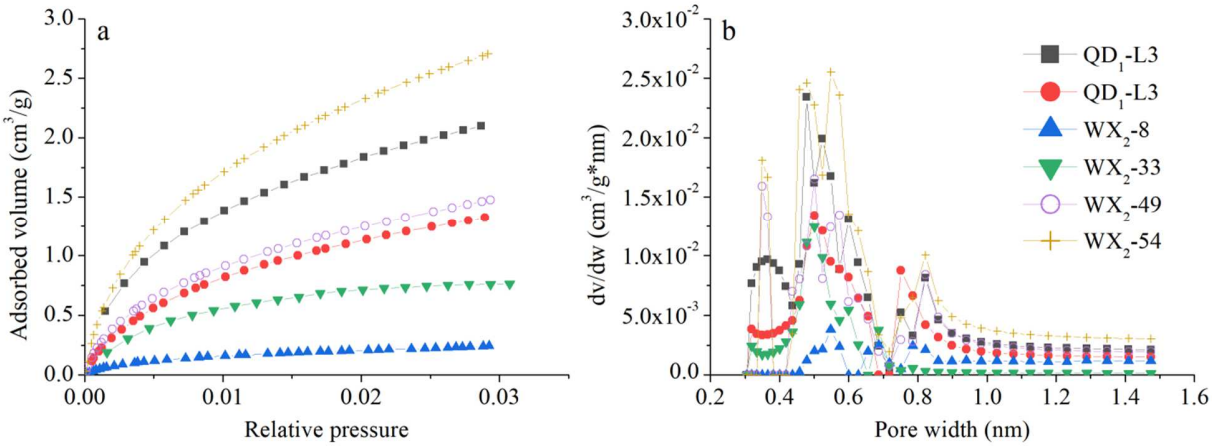

Figure 4. (a) Low-pressure CO_2 adsorption isotherms and **(b)** differential pore volume distributions.

4.3 Accessible and inaccessible nanopore characterization by SANS

Unlike MIP and LNA/LCA, SANS can probe both accessible and inaccessible pores in shales (Anovitz and Cole, 2015; Anovitz and Cole, 2019; Bahadur et al., 2014; Clarkson et al., 2013; Ruppert et al., 2013; Wang et al., 2018). Fig. 5a shows that the log of the scattering intensity, $I(Q)$, decreases with the increasing log of the scattering vector Q. Q and $I(Q)$ can be defined as (Glatter and Kratky, 1982):

$$Q = \frac{4\pi}{\lambda}\sin\theta \quad (1)$$

$$I(Q) = N(\Delta\rho^*)^2 \int V^2(r) f(r) P(Q,r) dr \quad (2)$$

where λ is the neutron wavelength; θ is the Bragg angle, which is the half of scattering angle; N is the pore number density; $(\Delta\rho^*)^2$ is the scattering contrast, which is equal to $\left(\rho_s^* - \rho_p^*\right)^2$, the square of the difference between the scattering length density (SLD) of the matrix and that of the pores (generally taken to be zero); $V(r)$ is the spherical volume; $f(r)$ is the pore size distribution; r is the spherical pore radius; and $P(Q,r)$ is the spherical form factor. The approximately linear relationship between $I(Q)$ and Q or $Q^4 I(Q)$ and Q indicates a fractal pore structure for the six shale samples (Fig. 5). Here, the pore size can be estimated by Bragg's law with Q as $r = \pi/Q$ in radius or $d = 2\pi/Q$ in diameter (Bragg, 1913). Sample WX_2-54 has the highest $I(Q)$ over the entire Q range, which suggests that it has the highest total pore volume and surface area (including open and closed pores) among the tested shale samples. Both samples WX_2-8 and WX_2-33 have relatively lower $I(Q)$s at Q > 0.01 $Å^{-1}$ than the other samples, indicating relatively low pore volumes and surface areas in the mesopore range. The approximately linear relationship between $\log(I(Q))$ and $\log(Q)$ or $\log(Q^4 I(Q))$ and $\log(Q)$ indicates that the six shale samples have a fractal pore structure (Fig. 5). The results of our previous study (Wang et al., 2018), showed that samples QD_1-L3, WX_2-8, and WX_2-33 exhibit surface fractal features with dimensionalities of 2.78, 2.42, and 2.84, respectively. In contrast, mass fractal features were found for samples QD_1-L4, WX_2-49, and WX_2-54, with fractal dimensions of 2.89, 2.93, and 2.84, respectively.

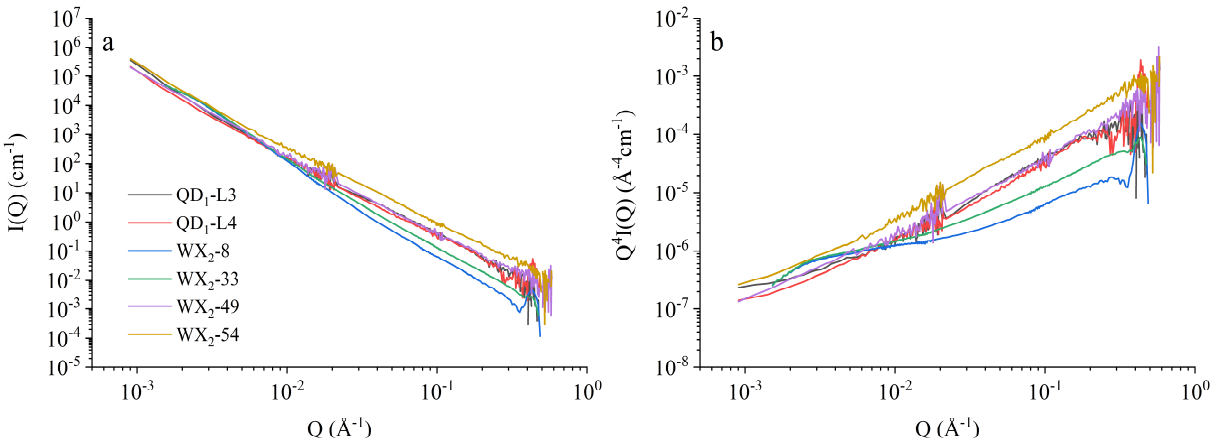

Figure 5. Background-subtracted scattering profiles in log-log plots: **(a)** $I(Q)$ versus Q and **(b)** $Q^4I(Q)$ versus Q.

We estimated the PSDs of the tested samples based by fitting of scattering intensity $I(Q)$ as a function of Q using three methods: (1) the polydisperse spherical pore (PDSP) model in PRINSAS (Hinde, 2004), as well as (2) the maximum entropy (MaxEnt) method (Ilavsky and Jemian, 2009), and (3) the total non-negative least square (TNNLS) method in IRENA (Ilavsky and Jemian, 2009). The assumption of spherical pore shape was used for each method. Note that, pore morphology is really complicated in the shale matrix, which can be found in the SEM images of the tested samples (Wang et al., 2018). Here, the spherical-shaped pore was used in SANS data analysis because of simplicity. The background-subtracted scattering intensity is shown in Eq. 2. Note that, $f(r) = \frac{r^{-(1+D)}}{(r_{\min}^{-D} - r_{\max}^{-D})/D}$ defines the fractal pore size distribution in PRINSAS, where D is the fractal dimension; $r_{\min}$ and $r_{\max}$ are the lower and upper limits of pore radius, respectively. However, $f(r)$ does not have a predefined functional form in the MaxEnt and TNNLS methods in IRENA. Values for $r_{\min}$ and $r_{\max}$ were automatically determined during fitting in PRINSAS, and the number of bins was set to be 30 for each decade of Q. In IRENA, however, the upper and lower limits of pore diameter were artificially set at 1 nm and 600 nm, and the total number of bins was set to 100.

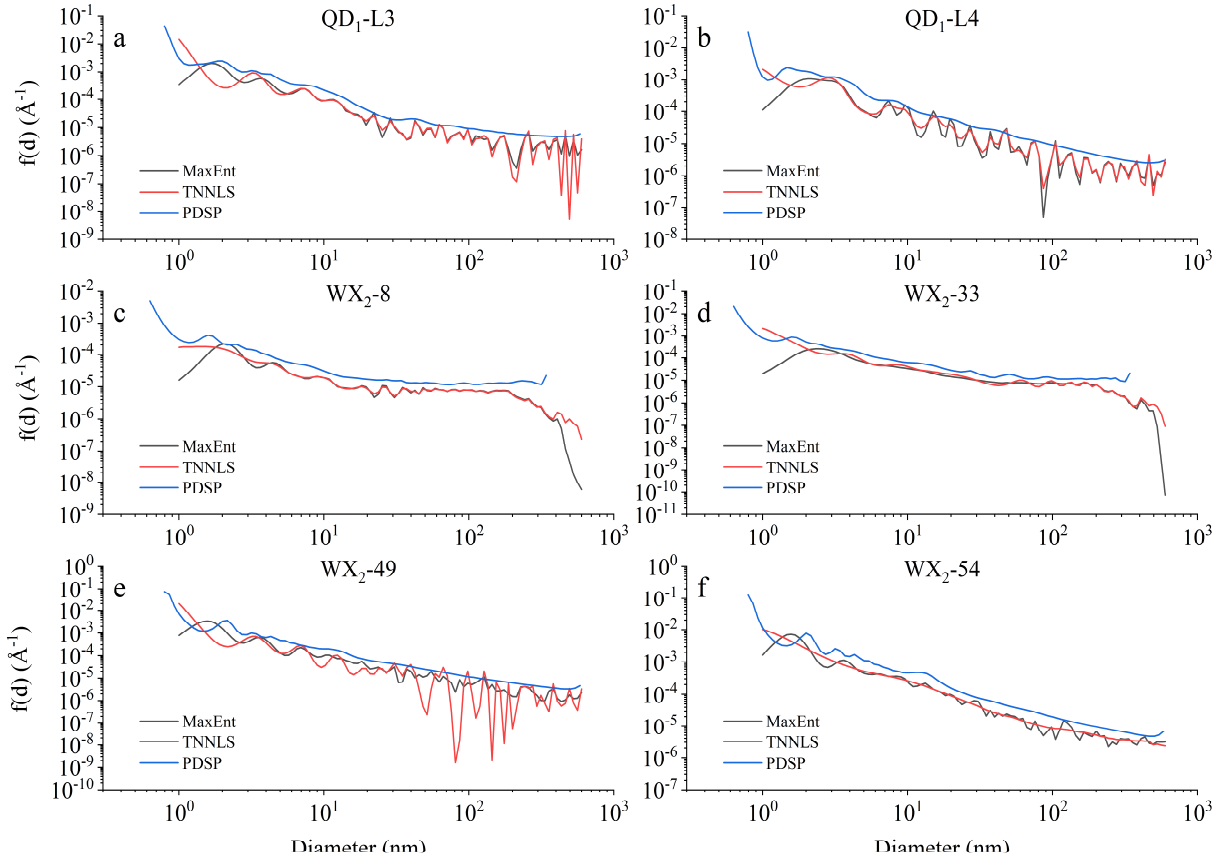

Figure 6. Comparison of PSDs estimated by different model fitting methods using scattering data for each shale sample: **(a)** QD_1-L3, **(b)** QD_1-L4, **(c)** WX_2-8, **(d)** WX_2-33, **(e)** WX_2-49, and **(f)** WX_2-54.

The estimated PSDs based on three model fitting methods are shown for each shale in Fig. 6. The different methods generally agreed well. The MaxEnt and TNNLS results are similar to each other, and the PDSP results are smoother and slightly higher than those from the other two methods. The discrepancy may be because PDSP contains a fractal functional form for pore size distributions, while MaxEnt and TNNLS do not have such an inherent constraint. The different sizes and numbers of bins used for the different models may also have affected the results. In addition, PDSP relates the pore size to the scattering vector as, $d = 5/Q$ (Radlinski et al., 2000), while MaxEnt and TNNLS use $d = 2\pi/Q$ (Bragg, 1913), which is derived from Eq. 1 and Bragg's law. For samples QD_1-L3 and WX_2-49, the TNNLS results are noisier (higher entropy) than the MaxEnt results, but this is weakly reversed for WX_2-54. This could be caused by

different error multipliers or the number of iterations used during the fitting, or may be inherent in the methods. Results from both the MaxEnt and TNNLS methods showed a significant decrease in pore number near the upper size limit for samples WX_2-8 and WX_2-33. This suggests that the upper pore size limit used (600 nm) is greater than the real maximum pore size limit for these two shales.

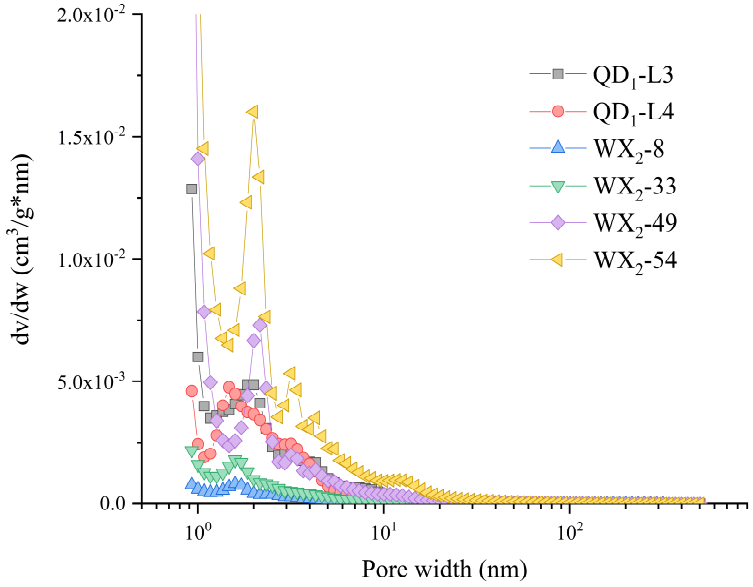

Figure 7. Comparison of differential pore volume distributions from the PDSP method using scattering data for the tested shale samples.

Fig. 7 shows a comparison of the estimated PSDs from the PDSP approach for the different samples. The profiles show bi- or multi-modal features. Sample WX_2-54 has the highest dV/dW, while samples WX_2-8 and WX_2-33 have lower values, which is consistent with the scattering profiles (Fig. 5) and the results from the fluid invasion methods (Figs. 2, 3, and 4). We found that the PSD has a peak with position around 2 nm for each shale sample. The PSD results differ from those from N_2 adsorption, which have no apparent 2 nm peak. This indicates either the existence of a considerable percentage of inaccessible pores or a substantial degree of heterogeneity at a pore size around 2 nm for the samples tested.

We estimated the pore volumes and surface areas in the mesopore range (2-50 nm) from the PSD results, and compared them with results from N_2 adsorption. These can be estimated as:

$$V = \frac{N}{\rho}\int f(r)V(r)dr \quad (3)$$

$$S = \frac{N}{\rho}\int f(r)A(r)dr \quad (4)$$

where N is the pore number density; ρ is the sample density; $V(r)$ is the spherical volume which equals to $4/3\pi r^3$; $A(r)$ is the spherical surface which equals to $4\pi r^2$. As can be seen in Table 2, the mesopore volumes estimated from the SANS data range between 0.26 and 3.42 $cm^3/100g$; Mesopore surface areas range between 2.39 and 43.62 m^2/g. These are significantly greater than those obtained from N_2 adsorption, suggesting that the samples contain some percentage of inaccessible pores. However, this "extra" scattering intensity could also arise from factors other than inaccessible porosity such as heterogeneity in the chemical composition or density of the shale matrix (Anovitz and Cole, 2015).

5. Discussion

5.1 Overall nanopore size distribution

A multi-scale PSD for each sample, including the micro-, meso- and macropore ranges, was obtained by combining PSDs estimated from MIP, LNA, LCA, and SANS as shown in Fig. 8. LCA and LNA access pore diameters ranging from 0.35 to 150 nm, SANS covers pore scales from 1.7 to 500 nm, and MIP accesses pore diameters from 3 to 15,000 nm. To provide a direct comparison, we have converted the PSD results of MIP, LCA, LNA, and SANS into unified units of $cm^3g^{-1}nm^{-1}$. In all of the samples analyzed, a significant portion of the nanopores fall into a size range between 0.35 and 100 nm. The PSDs in this size range derived from the LCA and SANS data agree well, except for those from samples WX_2-33 and WX_2-54 (Fig. 8d and f), where the PSD estimated by SANS is higher than that from LCA. This indicates the presence of

372 a poorly-connected micropore system in these two shales, leading to the presence of closed
373 porosity not detected by LCA. Similarly, the PSDs derived from SANS, LNA, and MIP appear
374 to be in reasonable agreement for most of the tested samples. However, there is an obvious
375 discrepancy between the SANS and MIP results at pore diameters in the 100-300 nm range for
376 samples QD_1-L3, WX_2-8, and WX_2-33 (Fig. 8a, c, and d), where the PSD estimated by SANS is
377 greater than that from MIP. This difference may reflect the existence of inaccessible porosity
378 (Clarkson et al., 2013; Zhang et al., 2015), or the heterogeneity of shale rock matrix (Table 1).
379 Additionally, the PSD estimated from the SANS data was unexpectedly lower than that
380 measured by MIP for sample WX_2-33 from 5 to 40 nm (Fig. 8d). One possible explanation for
381 this discrepancy is that compression of the shale sample at high mercury intrusion pressures may
382 have lead to alteration of the pore structure, a known drawback of MIP method (Clarkson and
383 Bustin, 1999; Rani et al., 2015). Since mercury can only be injected into accessible pores, there
384 may be more compression for samples with more inaccessible pores. Another possible reason
385 may be that the sample with higher calcite content (13.71% for WX_2-33) may have higher
386 compressive effect. In addition, heterogeneity of rock matrix may play a role in the results
387 between MIP and SANS.

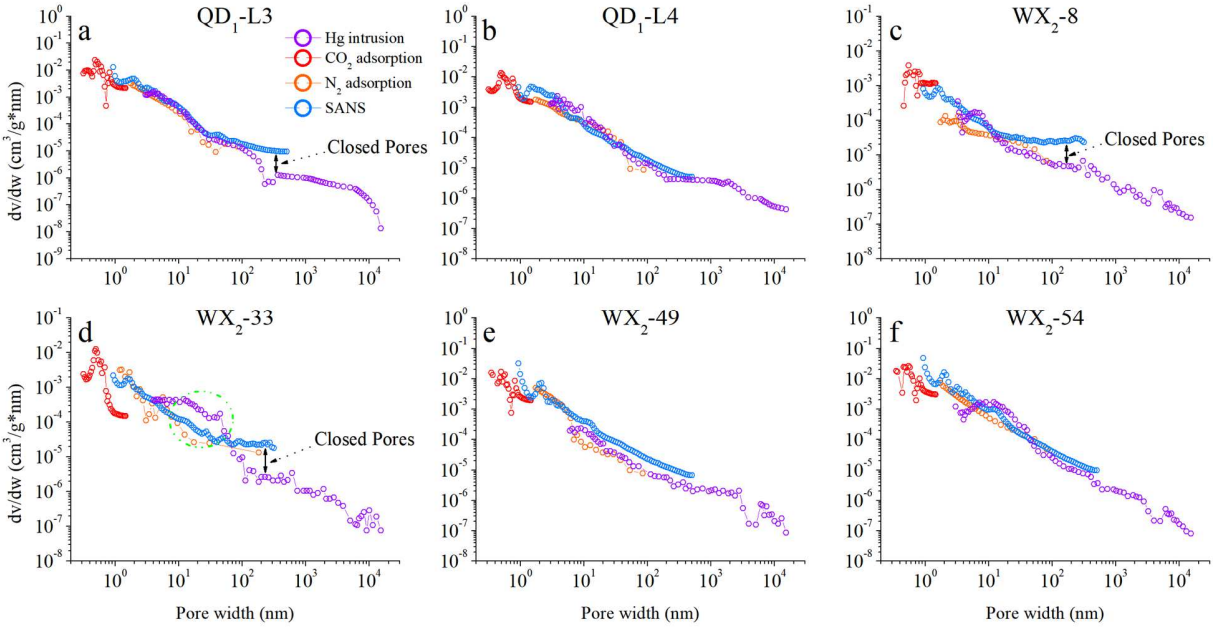

Figure 8. Overall pore size distribution from different techniques for **(a)** QD_1-L3, **(b)** QD_1-L4, **(c)** WX_2-8, **(b)** WX_2-33, **(e)** WX_2-49, and **(f)** WX_2-54.

5.2 Integration of pore volume and surface area in micro-/meso-/macropores

Based on the best performance window for each technique, MIP was used to quantify the pore volume and SSA of macropores (> 50 nm), and LNA and LCA were applied to quantify the pore volume and SSA of mesopores (2-50 nm) and micropores (< 2 nm) (Furmann et al., 2014; Mastalerz et al., 2013). SANS was used to quantify the pore volume and SSA of both the accessible and inaccessible mesopores up to 600 nm in this study. The results of the pore volume and SSA measurements from the different techniques are shown in Table 2. The contributions of micro-/meso-/macropores pore volumes and SSA to the overall pore volume and SSA from the invasive methods are illustrated in Fig. 9. Not surprisingly, the micropore size range is the major contributor to the total surface area, contributing between 64.90 and 75.98 % of the total for the tested samples (Fig. 9b). The contribution of mesopores to the total surface area averaged 32.41 %, and the contribution of macropores is less than ~1 %. Thus, the total surface area for

403 both Longmaxi and Niutitang shales are dominated by micro-/mesopores, which is in agreement
404 with previous studies (Tian et al., 2015; Wang et al., 2016).

405 In contrast, the micropore, mesopore and macropore volumes account for averages of 26.78,
406 32.28, and 40.94 % of the total pore volume, respectively (Fig. 9a). The average percentage of
407 pore volume thus increases with increasing pore size. For example, macropores make up a much
408 higher percentage of the total volume (~80 %) of sample WX_2-8 than of the other shales.
409 Samples WX_2-33 and WX_2-54 have similar micro-/meso-/macropore percentages, where the
410 percentages of pore volume between micro-/mesopores are comparable for these two samples,
411 despite the total pore volume of the sample WX_2-33 being four times smaller than that of the
412 sample WX_2-54 (Table 2). Sample WX_2-49 has about equal meso-/macropores pore volumes, a
413 smaller micropore volume percentage, a relatively large total pore volume (~3.08 cm^3/100g).

414 Unlike the four Longamxi shale samples, however, the two samples from the Niutitang
415 formation, QD_1-L3 and QD_1-L4, have a smaller volume percentage of macropores than micro-
416 /mesopores. A similar result was occasionally observed in a previous study (Tuo et al., 2016).
417 Such a pore structure suggests that, in these rocks, methane may be successfully stored in micro-
418 /mesopore networks, but it will be difficult to be transported out of the formation due to its
419 limited conductivity through the macropore network. This undeveloped macropore network may
420 explain why that there has been no commercialization of natural gas from the Niutitang
421 formation. On the other hand, previous studies have shown that the Niutitang shales developed
422 relatively fewer organic matter pores with smaller diameters and lower connectivity compared to
423 the Longmaxi shales (Wang et al., 2016; Zhao et al., 2016). The substantial differences in
424 organic matter pores between the two marine shale Formations may also influence gas
425 production.

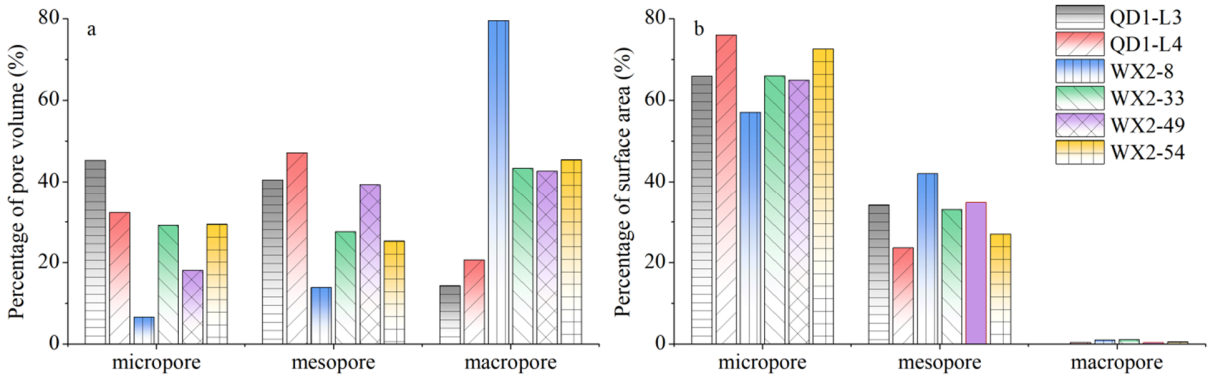

Figure 9. Comparison of **(a)** pore volume and **(b)** surface area contributions for micro-/meso-/macropores from invasive methods.

5.3 Correlations of pore properties with adsorption capacity and shale compositions

Correlations between pore properties, methane adsorption, and TOC and clay contents are shown in Fig. 10. There are reasonably strong correlations between micropore volume and SSA estimated by CO_2 adsorption and TOC (Fig. 10b and e), indicating that organic matter is a significant contributor to the shale micropore system. This is consistent with the results from other gas-mature shales in previous studies (Furmann et al., 2016; Milliken et al., 2013; Pan et al., 2015; Ross and Bustin, 2009; Yang et al., 2017). In contrast, there are negligible correlations between macropore properties estimated by MIP and TOC content (Fig. 10b and e). There are strong correlations between both mesopore volume and surface area estimated by SANS and TOC (R^2 = 0.90 for pore volume and R^2 = 0.92 for surface area), but relatively weaker relationships between the mesopore volume and surface area estimated by N_2 adsorption and TOC (R^2 = 0.55 for pore volume and R^2 = 0.70 for surface area). These results suggest that organic matter may have developed inaccessible mesopores within the shale matrix. This is consistent with focused ion beam-/SEM study (Nie et al., 2018; Yang et al., 2016), which show isolated pores forming in organic-filled regions.

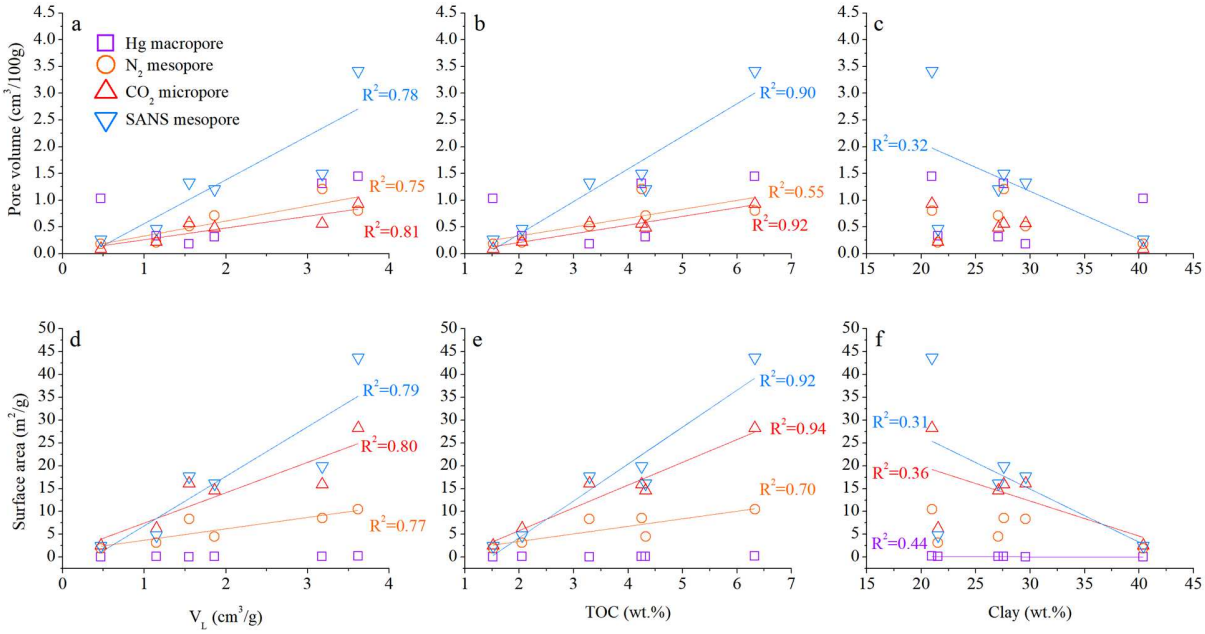

Figure 10. Correlations between methane adsorption amount and **(a)** pore volume and **(d)** surface area, between TOC content and **(b)** pore volume and **(e)** surface area, and between clay content and **(c)** pore volume and **(f)** surface area.

FE-SEM images from our previous study (Wang et al., 2018) show that these samples contain intraparticle pores (IntraP) in flocculated clay aggregates and interparticle pores (InterP) between clay mineral layers. However, as shown in Fig. 10c and f, the pore volumes and surface areas of micro-/meso-/macropores are almost independent of clay content, although there are weak correlations between the clay content and the MIP-estimated macropore surface area, the CO_2 adsorption-estimated micropore surface area, and the SANS-estimated mesopore volume/surface area. Clay minerals typically contain nanoscale pore structure, while clay mineral evolution may have a destructive effect on primary pores (Metwally and Chesnokov, 2012; Xiao et al., 2018). Thus, the lack of a correlation between the micro-, meso-, macropore volumes and surface areas and clay content in our samples may imply that clay minerals could play an essential role in the complexity of shale nanopore structure of Longmaxi and Niutitang formations.

As shown in Fig. 10a and d, methane adsorption capacity increases with increasing pore volume and surface area of micro-/mesopores. A detailed estimation of methane adsorption capacity was presented in our previous study (Wang et al., 2018), but these positive correlations suggest that the micro-/mesopore structures are governing factors in methane storage in these shale formations. As we have shown, to the extent that these six samples are representative, that organic matter is a controlling factor in the development of micro-/mesopores, the organic matter could also be an indicator of methane adsorption capacity in organic-rich marine shale gas reservoirs (Wang et al., 2018).

5.4 Characterization of mesopore connectivity

The estimated fractions of accessible mesopore volume and surface area, based on the SANS and LNA data, are shown in Fig. 11. Note that, the total pore volume and surface area of mesopores estimated by SANS assumed spherical pore shape; the accessible mesopore volume was estimated by BJH method, and the accessible mesopore surface area was approximately calculated by the subtraction of the BET surface area from the surface area of micro-/macropores. The fraction of accessible mesopore volume and surface area were estimated by:

$$F_{\mathrm{V}} = \frac{V_{\mathrm{BJH}}}{V_{\mathrm{SANS}}} \tag{5}$$

$$F_{\mathrm{S}} = \frac{S_{\mathrm{BET}} - S_{\mathrm{DA}} - S_{\mathrm{MIP}}}{S_{\mathrm{SANS}}} \tag{6}$$

where F_{V} and F_{S} are the fraction of accessible mesopore volume and surface area, respectively; V_{BJH} is the BJH mesopore volume from N_2 adsorption; V_{SANS} is the spherical mesopore volume from SANS; S_{BET} is the BET surface area; S_{DA} is the D-A micropore surface area from CO_2 adsorption; S_{MIP} is the macropore surface area from MIP; and S_{SANS} is the spherical mesopore surface area from SANS. From Fig. 11, sample WX_2-54 has the smallest fractions of accessible mesopore volume and surface area, although this sample has the highest total mesopore volume

and surface area among the samples tested, and the fractions of accessible mesopore volume and surface area are similar. The other shale samples, however, have different fractions of accessible mesopore volume and surface area. In samples QD_1-L3, WX_2-8, and WX_2-33 the fraction of accessible mesopore volume is lower than that for surface area. In contrast, the accessible mesopore volume fraction is higher than that of the surface area for QD_1-L4 and WX_2-49. These differences do not depend on the shale formation from which the samples were obtained.

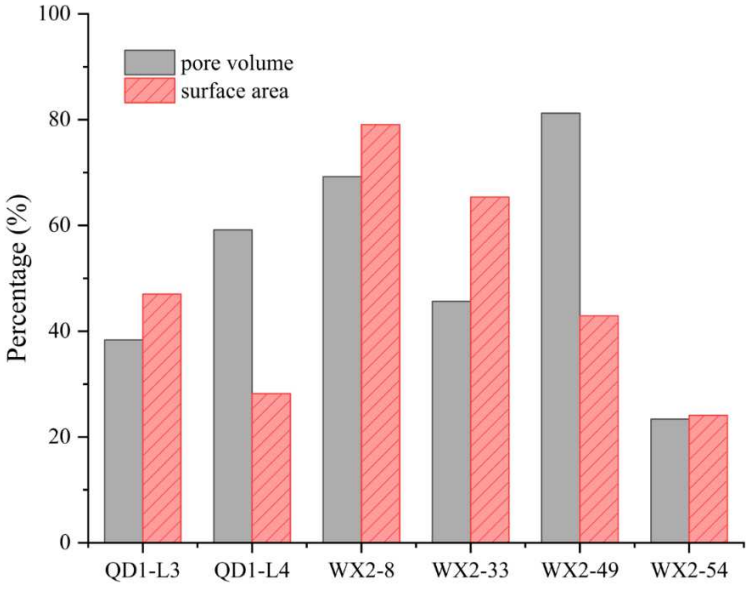

Figure 11. The fractions of accessible mesopore volume and surface area. The fraction of accessible mesopore volume is estimated from SANS and LNA data (Eq. 5). The fraction of accessible mesopore surface area is estimated from SANS, LNA, LCA, and MIP data (Eq. 6).

The relationships between the accessible mesopore volume and surface area and their percentage accessibilities are shown in Fig. 12, and the correlations between accessibility and adsorption capacity, TOC and clay contents are shown in Fig. 13. There is a negligible correlation between the BJH-estimated accessible mesopore volume and its percentage accessibility (Fig. 12a), and there are also no obvious correlations between accessibility and methane adsorption capacity or TOC (Fig. 13a and b). These results indicate that the fraction of accessible mesopore volume does not control the adsorption amount. However, percent

accessibility decreases with increasing BET-estimated accessible mesopore surface area (Fig. 12b), methane adsorption capacity, and TOC content (Fig. 13d and e). The results are consistent with the finding of our previous study (Wang et al., 2018), which suggested that high pore accessibility reduces total adsorption capacity due to relatively low surface area and TOC values.

In the previous section, it was suggested that the inaccessible mesopores could be located, at least in part, in the organic matter in the shale matrix. This is consistent with the strong negative correlation between the fraction of accessible mesopore surface area and TOC content, as shown in Fig. 13e. That is, the more TOC in the sample the smaller the fraction of the total mesopore surface area that is accessible. Thus, the degree of interconnectivity is much more strongly correlated with the surface area than the pore volume in the mesopore range. This suggests that the fraction of accessible mesopore surface area could be an indicator of gas transport and storage in organic mesopores. Samples with a higher fraction of mesopore surface area tend to have a lower gas-storage capability but a higher transport capability in organic matter, vice versa. In contrast, the correlations between the accessible fractions of both mesopore volume and surface area and clay content are weak (Fig. 13c and f), suggesting that clay content has minimal effect on the mesopore connectivity. Pores between clay packets may, therefore, be generally part of the connected pore matrix.

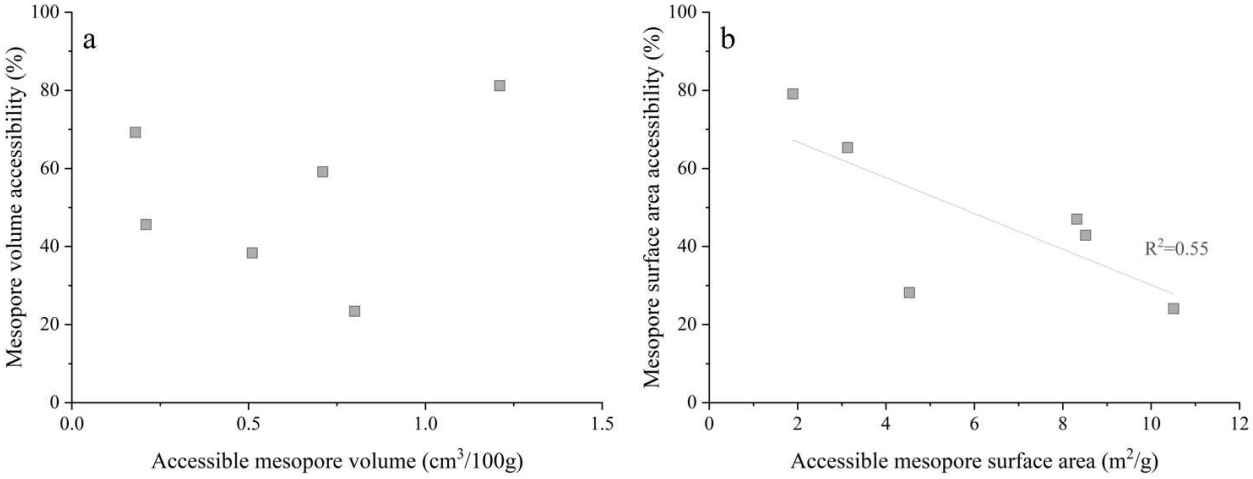

517

518 **Figure 12.** Correlations between mesopore **(a)** volume and **(b)** surface area and their accessibilities for all
519 shale samples.

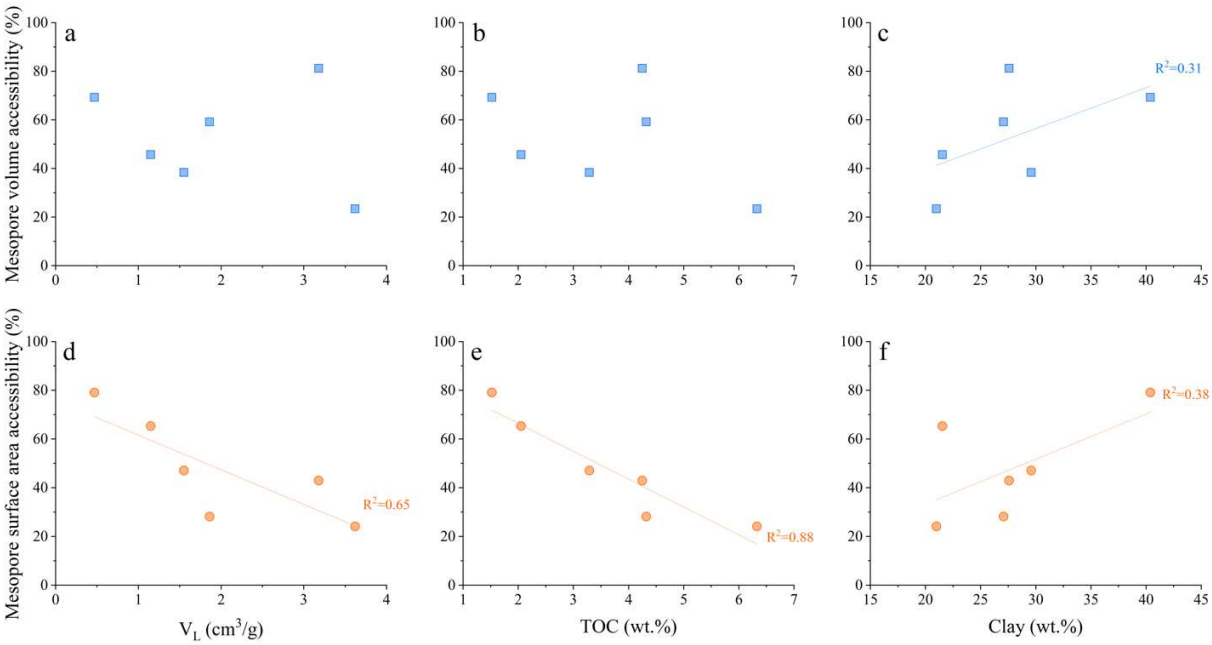

520

521 **Figure 13.** Correlations between methane adsorption capacity and the fractions of mesopore **(a)** volume and **(d)**
522 surface area, between TOC content and the fractions of mesopore **(b)** volume and **(e)** surface area, and between
523 clay content and the fractions of mesopore **(c)** volume and **(f)** surface area for all shale samples.

524 **6. Conclusions**

525 The multi-scale nanopore structure and mesopore connectivity of organic-rich marine shales

526 from the Upper Yangtze Platform in China were investigated using a series of techniques

527 including MIP, low-pressure N_2/CO_2 adsorption, and SANS. Based on the results of this
528 characterization, the following conclusions can be drawn:

529 (1) Based on the integration of MIP, low-pressure N_2/CO_2 adsorption, and SANS techniques,
530 there are uni-, bi-, and multi-modal PSDs over a wide pore size range (0.35-15,000 nm)
531 for both Longmaxi and Niutitang shales, and a significant portion of nanopores in these
532 samples fall in a size range between 0.35 and 100 nm.

533 (2) From the results of fluid-invasion methods (MIP, low-pressure N_2/CO_2 adsorption),
534 micro-scale pores are the major contributor to the total surface area for both Longmaxi
535 and Niutitang shales. Pore volume increases with increasing pore size for Longmaxi
536 shales, whereas Niutitang shales have more volume in the micropore and mesopore range
537 than in macropores.

538 (3) Organic matter is the primary contributor to the micropore system. Both micropores and
539 mesopores control the methane adsorption in the organic-rich shales.

540 (4) The fraction of accessible surface area of mesopores, estimated by comparing surface
541 areas in the mesopore range obtained by invasive methods to those obtained by SANS, is
542 an indicator of gas transport and storage in organic mesopores. Shale samples with higher
543 accessibility could have a higher capability for gas transport but lower gas storage
544 capacity, and vice versa.

545 **Acknowledgments**

546 The authors would like to acknowledge the financial support of the National Natural
547 Science Foundation of China (41802183, 41972169) and the National Science and Technology
548 Major Project (2017ZX05035004-002). Work by L.M. Anovitz was supported by the U.S.
549 Department of Energy, Office of Science, Office of Basic Energy Sciences, Chemical Sciences,

Geosciences, and Biosciences Division. This research used resources at the High Flux Isotope Reactor, a DOE Office of Science User Facility operated by the Oak Ridge National Laboratory. Access to NG7-SANS was provided by the Center for High-Resolution Neutron Scattering, a partnership between the National Institute of Standards and Technology and the National Science Foundation under Agreement No. DMR-1508249. Any opinions, findings, and conclusions or recommendations expressed in this study do not necessarily reflect the views of the U.S. Department of Energy, the National Institute of Standards and Technology or the National Science Foundation. The authors declare no competing financial interest.

References

Anovitz, L.M., Cole, D.R., 2019. Analysis of the pore structures of shale using neutron and X-ray small angle scattering. Geol. Carbon Storage 71-118.

Anovitz, L.M., Cole, D.R., 2015. Characterization and analysis of porosity and pore structures. Rev. Mineral. Geochem. 80(1), 61-164.

Anovitz, L.M., Lynn, G.W., Cole, D.R., Rother, G., Allard, L.F., Hamilton, W.A., Porcar, L., Kim, M., 2009. A new approach to quantification of metamorphism using ultra-small and small angle neutron scattering. Geochim. Cosmochim. Ac. 73(24), 7303-7324.

Bahadur, J., Ruppert, L.F., Pipich, V., Sakurovs, R., Melnichenko, Y.B., 2018. Porosity of the Marcellus Shale: A contrast matching small-angle neutron scattering study. Int. J. Coal Geol. 188, 156-164.

Bahadur, J., Melnichenko, Y.B., Mastalerz, M., Furmann, A., Clarkson, C.R., 2014. Hierarchical pore morphology of Cretaceous Shale: A small-angle neutron scattering and ultrasmall-angle neutron scattering study. Energy Fuels 28, 6336-6344.

Bragg, W. L., 1913. The diffraction of short electromagnetic waves by a crystal. Proc. Camb. Philos. Soc. 17, 43-57.

Carlson, E.S., Mercer, J.C., 1991. Devonian shale gas production: mechanisms and simple models. J. Petrol. Technol. 43(04), 476-482.

Chalmers, G.R.L., Bustin, R.M., Power, I.M., 2012. Characterization of gas shale pore systems by porosimetry, pycnometry, surface area, and field emission scanning electron microscopy/transmission electron microscopy image analyses: examples from the Barnett, Woodford, Haynesville, Marcellus, and Doig units. AAPG Bull. 96 (6), 1099-1119.

Chen, L., Jiang, Z., Liu K, Wang, P., Gao, F., Hu, T., 2017b. Application of low-pressure gas adsorption to nanopore structure characterization of organic-rich lower Cambrian shale in the Upper Yangtze Platform, South China. Aust. J. Earth Sci. 64(5), 653-665.

Chen, L., Jiang, Z., Liu K, Tan, J., Gao, F., Wang, P., 2017a. Pore structure characterization for organic-rich Lower Silurian shale in the Upper Yangtze Platform, South China: A possible mechanism for pore development. J. Nat. Gas Sci. Eng. 46, 1-15.

586 Cipolla, C.L., 2009. Modeling production and evaluating fracture performance in unconventional
587 gas reservoirs. J. Petrol. Technol. 61(09), 84-90.
588 Clarkson, C.R, Bustin, R.M., 1999. The effect of pore structure and gas pressure upon the
589 transport properties of coal: a laboratory and modeling study. 1. Isotherms and pore volume
590 distributions. Fuel 78(11), 1333-1344.
591 Clarkson, C.R., Solano, N., Bustin, R.M., Bustin, A.M.M., Chalmers, G.R.L., He, L.,
592 Melnichenko, Y.B., Radlinski, A.P., Blach, T.P., 2013. Pore structure characterization of
593 North American shale gas reservoirs using USANS/SANS, gas adsorption, and mercury
594 intrusion. Fuel, 103, 606-616.
595 Curtis, J.B., 2002. Fractured shale-gas systems. AAPG Bull. 86(11), 1921-1938.
596 Dai, J.X., Zou, C.N., Dong, D.Z., Ni, Y.Y., Wu, W., Gong, D.Y., Wang, Y.M., Huang, S.P.,
597 Huang, J.J., Fang, C.C., Liu, D., 2016. Geochemical characteristics of marine and terrestrial
598 shale gas in China. Mar. Petrol. Geol. 76, 444-463.
599 DiStefano, V.H., McFarlane, J., Stack, A.G., Perfect, E., Mildner, D.F.R., Bleuel, M., Chipera,
600 S.J., Littrell, K.C., Chershire, M.C., Manz, K.E., Anovitz, L.M., 2019. Solvent-pore
601 interactions in the Eagle Ford shale formation. Fuel, 238, 298-311.
602 Dubinin, M.M., 1989. Fundamentals of the theory of adsorption in micropores of carbon
603 adsorbents: characteristics of their adsorption properties and microporous structures. Pure
604 Appl. Chem. 61(11), 1841-1843.
605 Furmann, A., Mastalerz, M., Bish, D., Schimmelmann, A., Pedersen, P.K., 2016. Porosity and
606 pore size distribution in mudrocks from the Belle Fourche and Second White Specks
607 Formations in Alberta, Canada. AAPG Bull. 100(8), 1265-1288.
608 Furmann, A., Mastalerz, M., Schimmelmann, A., Pedersen, P.K., Bish, D., 2014. Relationships
609 between porosity, organic matter, and mineral matter in mature organic-rich marine
610 mudstones of the Belle Fourche and Second White Specks formations in Alberta, Canada.
611 Mar. Petrol. Geol. 54, 65-81.
612 Glatter, O., Kratky, O., 1982. Small angle X-ray scattering. Academic Press.
613 Gregg, S.J., Sing, K.S.W., 1982. Adsorption, Surface Area and Porosity, Academic Press,
614 London
615 Gu, X., Cole, D.R., Rother, G., Mildner, D.F.R., Brantley, S.L., 2015. Pores in Marcellus shale: a
616 neutron scattering and FIB-SEM study. Energy Fuels 29(3), 1295-1308.
617 Guo, T., 2016. Discovery and characteristics of the Fuling shale gas field and its enlightenment
618 and thinking. Earth Science Frontiers 23(1), 29-43 (in Chinese with English abstract).
619 Guo, T., Zhang, H., 2014. Formation and enrichment mode of Jiaoshiba shale gas field, Sichuan
620 Basin. Petrol. Explor. Dev. 41(1), 31-40.
621 Hazra, B., Wood, D.A., Vishal, V., Varma, A.K., Sakha, D., Singh, A.K., 2018. Porosity controls
622 and fractal disposition of organic-rich Permian shales using low-pressure adsorption
623 techniques. Fuel 220, 837-848.
624 Hinde, A.L., 2004. PRINSAS - a Windows-based computer program for the processing and
625 interpretation of small-angle scattering data tailored to the analysis of sedimentary rocks. J.
626 Appl. Crystallogr. 37, 1020-1024.
627 Ilavsky, J., Jemian, P.R., 2009. Irena: tool suite for modeling and analysis of small-angle
628 scattering. J J. Appl. Crystallogr. 42, 347-353.
629 Jarvie, D.M., Hill, R.J., Ruble, T.E., Pollastro, R.M., 2007. Unconventional shale-gas systems:
630 The Mississippian Barnett Shale of north-central Texas as one model for thermogenic shale-
631 gas assessment. AAPG Bull. 91(4), 475-499.

Jia, D., Wei, G., Chen, Z., Li, B., Zeng, Q., Yang, G., 2006. Longmen Shan fold-thrust belt and its relation to the western Sichuan Basin in central China: New insights from hydrocarbon exploration. AAPG Bull. 90(9), 1425-1447.
Kuila, U., Prasad, M., 2013. Specific surface area and pore-size distribution in clays and shales. Geophys. Prospect. 61(2), 341-362.
Lee, D.S., Herman, J.D., Elsworth, D., Kim, H.T., Lee, H.S., 2011. A critical evaluation of unconventional gas recovery from the marcellus shale, northeastern United States. KSCE J. Civ. Eng. 15(4), 679.
Li, J., Zhou, S., Li, Y., Ma, Y., Yang, Y., Li, C., 2016. Effect of organic matter on pore structure of mature lacustrine organic-rich shale: A case study of the Triassic Yanchang shale, Ordos Basin, China. Fuel 185, 421-431.
Liu, Y., Qiu, N., Xie, Z., Yao, Q., Zhu, C., 2016. Overpressure compartments in the central paleo-uplift, Sichuan Basin, southwest China. AAPG Bull. 100(5), 867-888.
Liu, Y., Yao, Y., Liu, D., Zheng, S., Sun, G., Chang, Y., 2018. Shale pore size classification: An NMR fluid typing method. Mar. Petrol. Geol. 96, 591-601.
Loucks, R.G., Reed, R.M., Ruppel, S.C., Hummes, U., 2012. Spectrum of pore types and networks in mudrocks and a descriptive classification for matrix-related mudrock pores. AAPG Bull. 96, 1071–1098.
Ma, Y., Zhang, S., Guo, T., Zhu, G., Cai, X., Li, M., 2008. Petroleum geology of the Puguang sour gas field in the Sichuan Basin, SW China. Mar. Petrol. Geol. 25(4-5), 357-370.
Mastalerz, M., Schimmelmann, A., Drobniak, A., Chen, Y., 2013. Porosity of Devonian and Mississippian New Albany Shale across a maturation gradient: Insights from organic petrology, gas adsorption, and mercury intrusion. AAPG Bull. 97(10), 1621-1643.
Mastalerz, M., Wei, L., Drobniak, A., Schieber, J., 2018. Responses of specific surface area and micro-and mesopore characteristics of shale and coal to heating at elevated hydrostatic and lithostatic pressures. Int. J. Coal Geol. 197, 20-30.
Meng, Q.R., Wang, E., Hu, J.M., 2005. Mesozoic sedimentary evolution of the northwest Sichuan basin: Implication for continued clockwise rotation of the South China block. Geol. Soc. Am. Bull. 117(3-4), 396-410.
Merkel, A., Fink, R., Littke, R., 2016. High pressure methane sorption characteristics of lacustrine shales from the Midland Valley Basin, Scotland. Fuel 182, 361-372.
Metwally, Y.M., Chesnokov, E.M., 2012. Clay mineral transformation as a major source for authigenic quartz in thermo-mature gas shale. Appl. Clay Sci. 55, 138-150.
Milliken, K.L., Rudnicki, M., Awwiller, D.N, Zhang, T., 2013. Organic matter–hosted pore system, Marcellus formation (Devonian), Pennsylvania. AAPG Bull. 97(2), 177-200.
Mohaghegh, S.D., 2013.Reservoir modeling of shale formations. J. Nat. Gas Sci. Eng. 12, 22-33.
Morga, R., Pawlyta, M., 2018.Microstructure of graptolite periderm in Silurian gas shales of Northern Poland. Int. J. Coal Geol. 189, 1-7.
Naveen. P., Asif, M., Ojha, K., 2018. Integrated fractal description of nanopore structure and its effect on CH_4 adsorption on Jharia coals, India. Fuel 232, 190-204.
Nie, H., Jin, Z., Zhang, J., 2018. Characteristics of three organic matter pore types in the Wufeng-Longmaxi Shale of the Sichuan Basin, Southwest China. Sci. Rep. 8(1), 7014.
Pan, J., Niu, Q., Wang, K., Shi, X., Li, M., 2016. The closed pores of tectonically deformed coal studied by small-angle X-ray scattering and liquid nitrogen adsorption. Micropor. Mesopor. Mat. 224, 245-252.

677 Pan, L., Xiao, X., Tian, H., Zhou, Q., Chen, J., Li, T., Wei, Q., 2015. A preliminary study on the
678 characterization and controlling factors of porosity and pore structure of the Permian shales
679 in Lower Yangtze region, Eastern China. Int. J. Coal Geol. 146, 68-78.
680 Pashin, J.C., Kopaska-Merkel, D.C., Arnold, A.C., Mclntyre, M.R., Thomas, W.A., 2012.
681 Gigantic, gaseous mushwads in Cambrian shale: Conasauga Formation, southern
682 Appalachians, USA. Int. J. Coal Geol. 103, 70-91.
683 Pearce, J.K., Dawson, G.K.W., Blach, T.P., Bahadur, J., Melnichenko, Y.B., Golding, S.D.,
684 2018b. Impure CO_2 reaction of feldspar, clay, and organic matter rich cap-rocks: Decreases
685 in the fraction of accessible mesopores measured by SANS. Int. J. Coal Geol. 185, 79-90.
686 Pearce, J.K., Turner, L., Pandey, D., 2018a. Experimental and predicted geochemical shale-water
687 reactions: Roseneath and Murteree shales of the Cooper Basin. Int. J. Coal Geol. 187, 30-44.
688 Radliński, A.P., Boreham, C.J., Lindner, P., Randl, O., Wignall, G.D., Hinde, A., Hope, J.M.,
689 2000. Small angle neutron scattering signature of oil generation in artificially and naturally
690 matured hydrocarbon source rocks. Org. Geochem. 31(1), 1-14.
691 Rani, S,. Prusty, B.K., Pal, S.K., 2015. Methane adsorption and pore characterization of Indian
692 shale samples. Journal of unconventional oil and gas resources 11, 1-10.
693 Romero-Sarmiento, M.F., Rouzaud, J.N., Bernard, S., Deldicque, D., Thomas, M., Littke, R.,
694 2014. Evolution of Barnett Shale organic carbon structure and nanostructure with increasing
695 maturation. Org. Geochem. 71, 7-16.
696 Ross, D.J.K., Bustin, R.M., 2009. The importance of shale composition and pore structure upon
697 gas storage potential of shale gas reservoirs. Mar. Petrol. Geol. 26(6), 916-927.
698 Ruppert, L.F., Sakurovs, R., Blach, T.P., He, L., Melnichenko, Y.B., Mildner, D.F.R., Alcantar-
699 Lopez, L., 2013. A USANS/SANS study of the accessibility of pores in the Barnett Shale to
700 methane and water. Energy Fuels 27, 772-779.
701 Sing, K.S., 1985. Reporting physisorption data for gas/solid systems with special reference to the
702 determination of surface area and porosity. Pure Appl. Chem. 57, 603–619.
703 Sun, M., Yu, B., Hu, Q., Chen, S., Xia, W., Ye, R., 2016. Nanoscale pore characteristics of the
704 Lower Cambrian Niutitang Formation Shale: a case study from Well Yuke# 1 in the
705 Southeast of Chongqing, China. Int. J. Coal Geol. 154, 16-29.
706 Sun, M., Yu, B., Hu, Q., Zhang, Y., Li, B., Yang, R., 2017. Pore characteristics of Longmaxi
707 shale gas reservoir in the Northwest of Guizhou, China: Investigations using small-angle
708 neutron scattering (SANS), helium pycnometry, and gas sorption isotherm. Int. J. Coal Geol.
709 171, 61-68.
710 Sun, M., Yu, B., Hu, Q., Yang, R., Zhang, Y., Li, B., Melnichenko, Y.B., Cheng, G., 2018. Pore
711 structure characterization of organic-rich Niutitang shale from China: Small angle neutron
712 scattering (SANS) study. Int. J. Coal Geol. 186, 115-125.
713 Tang, X., Jiang, S., Jiang, Z., Li, Z., He, Z., Long, S., Zhu, D., 2019. Heterogeneity of Paleozoic
714 Wufeng-Longmaxi formation shale and its effects on the shale gas accumulation in the Upper
715 Yangtze Region, China. Fuel, 239, 387-402.
716 Thommes, M., Kaneko, K., Neimark, A.V., Olivier, J.P., Rodriguez-Reinoso, F., Rouquerol, J.,
717 Sing, K.S., 2015. Physisorption of gases, with special reference to the evaluation of surface
718 area and pore size distribution (IUPAC Technical Report). Pure Appl. Chem. 87(9-10), 1051-
719 1069.
720 Tian, H., Pan, L., Zhang, T., Xiao, X., Meng, Z., Huang, B., 2015. Pore characterization of
721 organic-rich lower Cambrian shales in Qiannan depression of Guizhou province,
722 Southwestern China. Mar. Petrol. Geol. 62, 28-43.

723 Topór, T., Derkowski, A., Ziemiański, P., Szczurowski, J., McCarty, D.K., 2017. The effect of
724 organic matter maturation and porosity evolution on methane storage potential in the Baltic
725 Basin (Poland) shale-gas reservoir. Int. J. Coal Geol. 180, 46-56.
726 Tuo, J., Wu, C., Zhang, M., 2016. Organic matter properties and shale gas potential of Paleozoic
727 shales in Sichuan Basin, China. J. Nat. Gas Sci. Eng. 28, 434-446.
728 Wang, P., Jiang, Z., Chen, L., Yin, L., Li, Z., Zhang, C., Tang, X., Wang, G., 2016. Pore
729 structure characterization for the Longmaxi and Niutitang shales in the Upper Yangtze
730 Platform, South China: Evidence from focused ion beam–He ion microscopy, nano-
731 computerized tomography and gas adsorption analysis. Mar. Petrol. Geol. 77, 1323-1337.
732 Wang, Y., Qin, Y., Zhang, R., He, L., Anovitz, L.M., Bleuel, M., Mildner, D.F.R., Liu, S., Zhu,
733 Y., 2018. Evaluation of nanoscale accessible pore structure for improved prediction of gas
734 production potential in Chinese marine shales. Energy Fuels 2018, 32(12), 12447-12461.
735 Wang, Y., Zhu, Y., Chen, S., Li, W., 2014. Characteristics of the nanoscale pore structure in
736 Northwestern Hunan shale gas reservoirs using field emission scanning electron microscopy,
737 high-pressure mercury intrusion, and gas adsorption. Energy Fuels 28(2), 945-955.
738 Washburn, E.W., 1921. Note on a method of determining the distribution of pore sizes in a
739 porous material. Proceedings of the National Academy of Sciences 7(4), 115-116.
740 Webber, J.B.W., Corbett, P., Semple, K.T., Ogbonnaya, U., Teel, W.S., Masiello, C.A., Fisher,
741 Q.J., Valenza II, J.J., Song, Y., Hu, Q., 2013. An NMR study of porous rock and biochar
742 containing organic material. Micropor. Mesopor. Mat. 178, 94-98.
743 Wu, K., Chen, Z., Li, X., Guo, C., Wei, M., 2016. A model for multiple transport mechanisms
744 through nanopores of shale gas reservoirs with real gas effect–adsorption-mechanic coupling.
745 Int. J. Heat Mass Tran. 93, 408-426.
746 Wu, Y.S, Li, J., Ding, D., Wang, C., Di, Y., 2014. A generalized framework model for the
747 simulation of gas production in unconventional gas reservoirs. SPE J. 19(05), 845-857.
748 Xiao, D., Jiang, S., Thul, D., Lu, S., Zhang, L., Li, B., 2018. Impacts of clay on pore structure,
749 storage and percolation of tight sandstones from the Songliao Basin, China: Implications for
750 genetic classification of tight sandstone reservoirs. Fuel 211, 390-404.
751 Xiao, X.M., Wei, Q., Gai, H.F., Li, T.F., Wang, M.L., Pan, L., Chen, J., Tian, H. 2015. Main
752 controlling factors and enrichment area evaluation of shale gas of the Lower Paleozoic
753 marine strata in south China. Petrol. Sci. 12(4), 573-86.
754 Yang, R., Hao, F., He, S., He, C., Guo, X., Yi, J., Hu, H., Zhang, S., Hu, Q., 2017. Experimental
755 investigations on the geometry and connectivity of pore space in organic-rich Wufeng and
756 Longmaxi shales. Mar. Petrol. Geol. 84, 225-242.
757 Yang, R., He, S., Yi, J., Hu, Q., 2016. Nano-scale pore structure and fractal dimension of
758 organic-rich Wufeng-Longmaxi shale from Jiaoshiba area, Sichuan Basin: Investigations
759 using FE-SEM, gas adsorption and helium pycnometry. Mar. Petrol. Geol. 70, 27-45.
760 Zhang, L., Lu, S., Xiao, D., Li, B., 2017. Pore structure characteristics of tight sandstones in the
761 northern Songliao Basin, China. Mar. Petrol. Geol. 88, 170-180.
762 Zhang, R., Liu, S.M., Bahadur, J., Elsworth, D., Melnichenko, Y., He, L.L., Wang, Y., 2015.
763 Estimation and modeling of coal pore accessibility using small angle neutron scattering. Fuel
764 161, 323-332.
765 Zhao, W.Z., Li, J.Z., Yang, T., Wang, S.F., Huang, J.L., 2016. Geological difference and its
766 significance of marine shale gases in South China. Petrol. Explor. Dev. 43(4), 547-559.
767 Zhou, B., Han, Q., Yang, P., 2016. Characterization of Nanoporous Systems in Gas Shales by
768 Low Field NMR Cryoporometry. Energy Fuels 30(11), 9122-9131.

769 Zou, C.N., Dong, D.Z., Wang, Y.M., Li, X.J., Huang, J.L., Wang, S.F., Guan, Q.Z., Zhang, C.C.,
770 Wang H.Y., Liu, H.L., Bai, W.H., Liang F., Lin, W., 2015. Shale gas in China:
771 Characteristics, challenges and prospects (I). Petrol. Explor. Dev. 42(6), 753-767.